Tissue-Type Classification With Uncertainty Quantification of Microwave and Ultrasound Breast Imaging: A Deep Learning Approach

PEDRAM MOJABI[iD]**, VAHAB KHOSHDEL, (Student Member, IEEE), AND JOE LOVETRI**[iD]**, (Senior Member, IEEE)**
Department of Electrical and Computer Engineering, University of Manitoba, Winnipeg, MB R3T 5V6, Canada
Corresponding author: Pedram Mojabi (pedram.mojabi@gmail.com)

ABSTRACT A deep learning approach is proposed for performing tissue-type classification of tomographic microwave and ultrasound property images of the breast. The approach is based on a convolutional neural network (CNN) utilizing the U-net architecture that also quantifies the uncertainty in the classification of each pixel. Quantitative tomographic reconstructions of dielectric properties (complex-valued permittivity), ultrasonic properties (compressibility and attenuation), as well as their combination, with the corresponding actual tissue-type classification constitute the training set. The CNN learns to map the quantitative property reconstructions to a single tissue-type image. The level of confidence in predicting a tissue-type at each pixel is determined. This uncertainty quantification is diagnostically critical for biomedical applications, especially when attempting to distinguish between cancerous and healthy tissues. The Gauss-Newton Inversion algorithm is used for the quantitative reconstruction of both dielectric and ultrasonic properties. Electromagnetic and ultrasound scattered-field data is obtained from MRI-derived numerical breast phantoms. Several numerical breast phantoms types, from fatty to dense, are considered. The proposed classification and uncertainty quantification approach is shown to outperform a previously studied tissue-type classification method based on a Bayesian approach.

INDEX TERMS Tissue classification, uncertainty quantification, deep learning method, convolutional neural network, microwave tomography, ultrasound tomography, multi-physics imaging, inverse scattering, breast imaging.

I. INTRODUCTION

Microwave tomography (MWT) and ultrasound tomography (UT) are imaging modalities aiming to create quantitative or qualitative images of the dielectric or ultrasonic properties of an object-of-interest (OI) [1]–[19]. These images can be used for different applications such as industrial non-destructive testing or biomedical imaging. Quantitative dielectric properties of interest are the real and imaginary parts of the relative complex-valued permittivity related to the dielectric constant and the conductivity of the OI. Typical quantitative ultrasonic properties that can be recovered are the compressibility, attenuation, density and sound speed.

Different reconstruction algorithms can be utilized to create quantitative dielectric and ultrasonic properties of the OI such as ray-based methods, the Born-iterative method, as well as the Contrast-Source Inversion (CSI) and Gauss-Newton Inversion (GNI) algorithms. [8], [9], [19]–[24]. In this study, GNI is used as the full-wave reconstruction algorithm for both MWT and UT.

Having quantitative images of different physical properties of an OI can be beneficial, as one tissue-type may be well distinguished using one property whereas other tissues may be better distinguished in other properties [25]. However, it is more convenient for end-users (medical doctors for biomedical imaging applications) to be provided with a single image having each pixel interpreted as being a single tissue (with a certainty factor included). Such an image is called a tissue-type image (TTI) that is created

---

The associate editor coordinating the review of this manuscript and approving it for publication was Abhishek K. Jha[iD].

P. Mojabi *et al.*: Tissue-Type Classification With Uncertainty Quantification of Microwave and Ultrasound Breast Imaging

IEEE *Access*

using a classification algorithm's "interpretation" of available property images. The quantification of the classification algorithm's uncertainty in choosing a tissue for each pixel is also very crucial for medical doctors because sometimes artifacts may arise in some or all of the property images that make the assignment of a tissue difficult. If the confidence is high, it means that the medical doctors can have more trust that the chosen tissue-type for that pixel is correct. In the low confidence case, they may choose to implement other diagnostic methods.

The concept of creating composite tissue type images along with the uncertainty quantification (probability image) for ultrasound and microwave imaging was presented for the first time in [25]. Bayesian decision theory was used in that work to classify different tissues as well as to create an associated probability image that quantified the uncertainty. In that method, it is assumed that property values for each tissue are available and that the probability density functions or multivariate probability density function, describing the range of property values for each tissue, can be estimated [25]. The experimental validation of this method for both ultrasound and microwave imaging for a tissue mimicking phantom and a human forearm was presented in [1].

Deep learning methods have recently been investigated for biomedical imaging and inverse problems [26]–[37]. For example, a deep learning method was used to improve the quantitative reconstruction of microwave imaging in [27], [32]. The use of a Convolutional Neural Network (CNN) to learn the complex mapping from Magnetic Resonance (MR) images to dielectric images which is used as prior information for the microwave inverse scattering algorithms was considered in [28]. The segmentation of brain tumors based on contrast enhanced T1-weighted magnetic resonance imaging (MRI) was reported in [33]. A deep learning method for the classification of benign and malignant lung nodules on chest CT images is presented in [34]. In [35], a deep neural network architecture is utilized to map the image obtained from the low-resolution back-propagation method to a higher resolution result in the electromagnetic inverse scattering problem. Solving a full-wave inverse scattering problems using a CNN technique under different scenarios is presented in [29]. For example, complex scattered-field data are directly used as the input of a CNN to create dielectric properties of the OI in one of the scenarios proposed in [29].

Convolutional Neural Networks were typically designed for classification tasks [38], [39]. In this case, the input of the CNN is an image and the output is a label for the class member. In some applications such as image segmentation, it is required that the typical architecture of CNNs is changed in such a way that the output of CNN is also an image instead of a label for the class member. One of the well-known architectures proposed to create images as the output of CNN (as opposed to labels) is U-net [26]. This architecture was originally utilized for the segmentation of neuronal structures
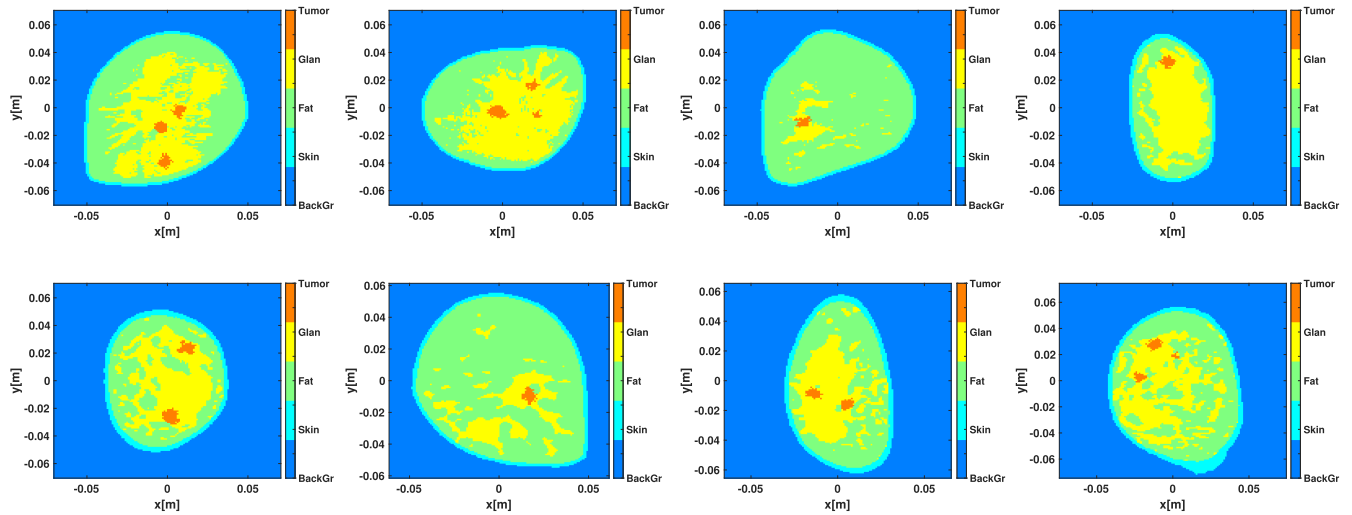
in electron microscopic recordings and cell segmentation in light microscopic images [26].

In this paper, a CNN with the U-net architecture is utilized to create a TTI along with the uncertainty quantification. The U-net architecture is modified for this application and it is trained based on a set of quantitative reconstructions of the dielectric and/or ultrasonic properties of several numerical phantoms and the true TTI corresponding to each of the reconstructions. Several numerical MRI-based breast phantoms are used in this work for creating the training and testing data sets [4], [40], [41]. The structure of this paper is as follows. In Section II, the training and testing date-sets for the U-net are described. The microwave and ultrasound scattered-field data-acquisition set-ups, problem formulations, and non-linear inversion algorithms are briefly described in Subsections II-A and II-B. The particular U-net architecture utilized for creating the uncertainty quantification image and TTI is presented in Section III. Results of testing the U-net for tissue classification and uncertainty quantification using MRI-based numerical breast phantoms are presented and discussed in Section IV. Finally, conclusions are presented in Section V.

II. TRAINING AND TESTING DATA SETS

To create training and testing data sets for our deep learning network, we start with eight tumorless MRI-derived numerical breast models that are segmented into four regions: the background, skin, fat, and fibroglandular regions. Five of the eight models are obtained from 2D tomographic MRI intensity images whereas the remaining three models are obtained from cross-sections of 3D MRI intensity images. Fifty different cross-sections are used from each of the three 3D models. These models represent all three of the main types of breast (dense, heterogeneously-dense and fatty). Randomized tumors of different sizes and at different locations are introduced into these models as follows. For each of the 2D-MRI derived models, we generate 50 cases containing one to three tumors within the fibroglandular region using a procedure similar to what was presented in [27]. Thus, these 250 cases have five different base-models (the top four and the left-most model on the second row of Fig 1). In each of the 50 cross-sections of each of the three 3D MRI intensity models, we introduce one set of tumors (a set being one to three tumors). This gives us 150 cases obtained from three 3D MRI intensity models and 250 cases from five 2D MRI intensity models, for a total 400 numerical breast phantoms containing one to three randomized tumors. We refer to our data-set as containing 50 tumor cases from 8 different models, although 150 of the cases obtained from the 3D MRI breast models have different fibroglandular regions (coming from different cross-sections of the 3D model).

The 400 numerical breast phantoms are segmented into the background region plus four tissue-type regions: skin, fat, fibroglandular, and tumor (as shown in Fig 1). These 400 MRI tomographic intensity phantoms are then filled with the dielectric and ultrasonic properties of the breast.

IEEE *Access*

P. Mojabi *et al.*: Tissue-Type Classification With Uncertainty Quantification of Microwave and Ultrasound Breast Imaging

FIGURE 1. The tissue type image of eight models of numerical MRI based breast phantoms utilized for training and testing of the deep learning network.

For example, the true TTI and images with the corresponding dielectric properties (*i.e.*, real and imaginary parts of the relative complex-valued permittivity denoted by ϵ_r and ϵ_i) and ultrasonic properties (*i.e.*, compressibility and attenuation denoted by κ and α) for five numerical breast phantoms are illustrated in Fig 3. It should be noted that none of the fifty phantoms for a particular model have been used for training the U-net when one of the phantoms of that model is chosen as a test-case for the deep learning network. This corresponds to an eight-fold cross-validation procedure (*i.e.*, one of the eight groups of fifty is removed from the training set when a test case from that group is used for testing).

A. MWT AND UT SCATTERED FIELD FORMULATION

In non-linear inversion algorithms, the unknown contrasts related to the dielectric and ultrasonic properties can be found by iteratively minimizing the discrepancy between the measured and simulated scattered electric and pressure fields. The simulated scattered field is defined as the subtraction of the incident field (*i.e.*, the field in the absence of the OI) from total field (*i.e.*, the field in the presence of the OI). The simulated scattered pressure for the inhomogeneous compressibility and attenuation can be found as [9], [19], [21]

$$p^{scat}(\mathbf{r}) = k_0^2 \int_D g(\mathbf{r}, \mathbf{r}')\chi_1^c(\mathbf{r}')p(\mathbf{r}')d\mathbf{r}' \qquad (1)$$

where k_0 and $g(\mathbf{r}, \mathbf{r}')$ are the background wavenumber and Green's function of the background medium. Also, $\chi_1^c(\mathbf{r})$ is the complex contrast of compressibility defined as

$$\chi_1^c(\mathbf{r}) \triangleq \frac{\kappa(\mathbf{r}) - \kappa_b}{\kappa_b} - j\frac{2\delta\alpha(\mathbf{r})}{k_0} \qquad (2)$$

where $\delta\alpha(\mathbf{r})$ is defined as the subtraction of the background attenuation from the attenuation at position $\mathbf{r}$. Also, $\kappa(\mathbf{r})$ and κ_b are the compressibility at position $\mathbf{r}$ and the

compressibility of the background medium. The variation of density is neglected in the above scattered pressure equation.

The simulated scattered electric field for the inhomogeneous permittivity and conductivity is obtained as [42]

$$E^{scat}(\mathbf{r}) = k_0^2 \int_D g(\mathbf{r}, \mathbf{r}')\chi(\mathbf{r}')E(\mathbf{r}')d\mathbf{r}' \qquad (3)$$

where $\chi(\mathbf{r})$ is the complex permittivity contrast defined as

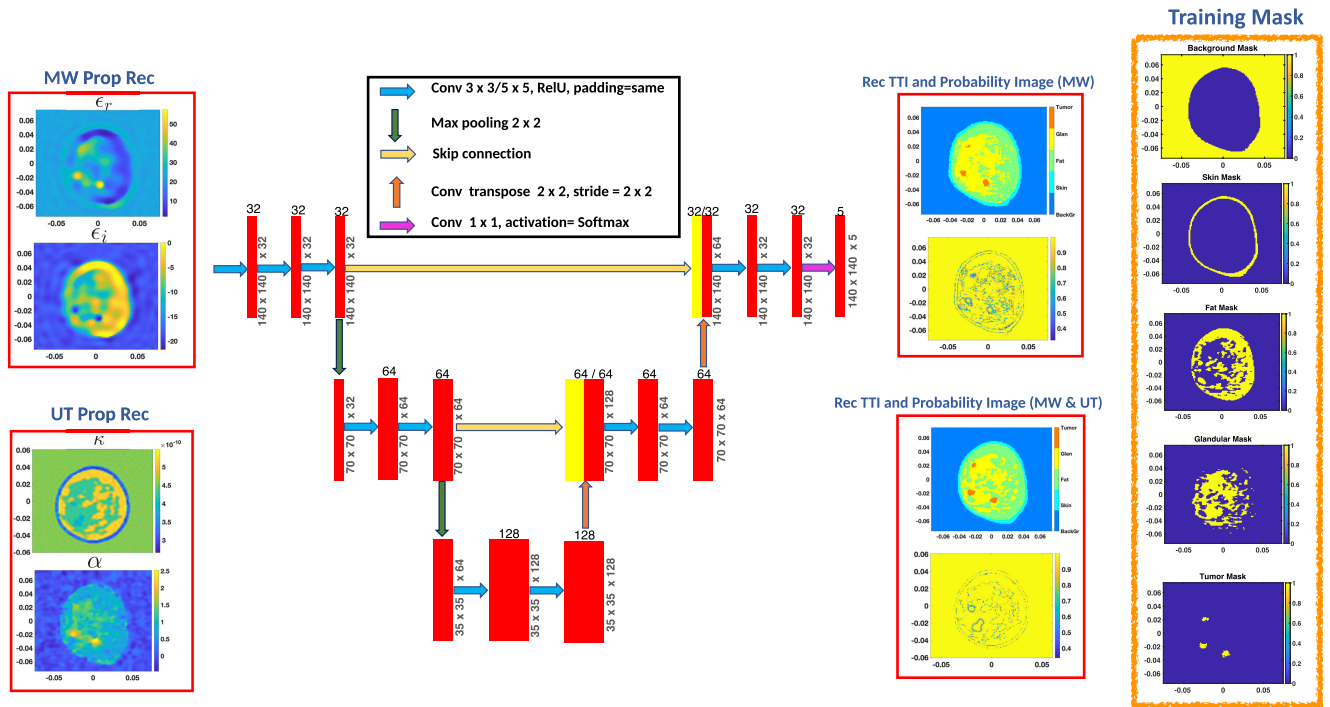$$\chi(\mathbf{r}) \triangleq \frac{\epsilon_r(\mathbf{r}) - \epsilon_b}{\epsilon_b} \qquad (4)$$

and $\epsilon_r(\mathbf{r})$ and ϵ_b are the complex permittivity at position $\mathbf{r}$ and the background complex permittivity.

B. RECONSTRUCTION SETUP FOR MWT AND UT

The Gauss-Newton inversion is used as the non-linear inversion algorithm to reconstruct both dielectric and ultrasonic properties of the OI [20]. It should be noted that the variation of density considered in [5], [21] is neglected for the UT reconstructions. The scattered-field data used to create ultrasonic and dielectric properties of the OI for all examples used in training the CNN is contaminated with five percent noise [43]. The OI is surrounded by 30 and 64 transceivers for MWT and UT, respectively. These transceivers are positioned in a circle having a radius of 12 [cm]. It is assumed that the relative complex permittivity of the background medium for MWT is $23.3 - j18.46$ [44] and water is used as a background medium for UT. Three frequencies of operation are simultaneously used for the reconstruction of object properties. These frequencies for MWT are $f = [1, 1.5, 2]$ GHz and for UT are $f = [100, 130, 160]$ kHz.

III. DEEP LEARNING FOR TISSUE CLASSIFICATION AND UNCERTAINTY QUANTIFICATION

The CNN U-net architecture originally proposed in [26] for segmentation of neuronal structures in electron microscopic

P. Mojabi *et al.*: Tissue-Type Classification With Uncertainty Quantification of Microwave and Ultrasound Breast Imaging
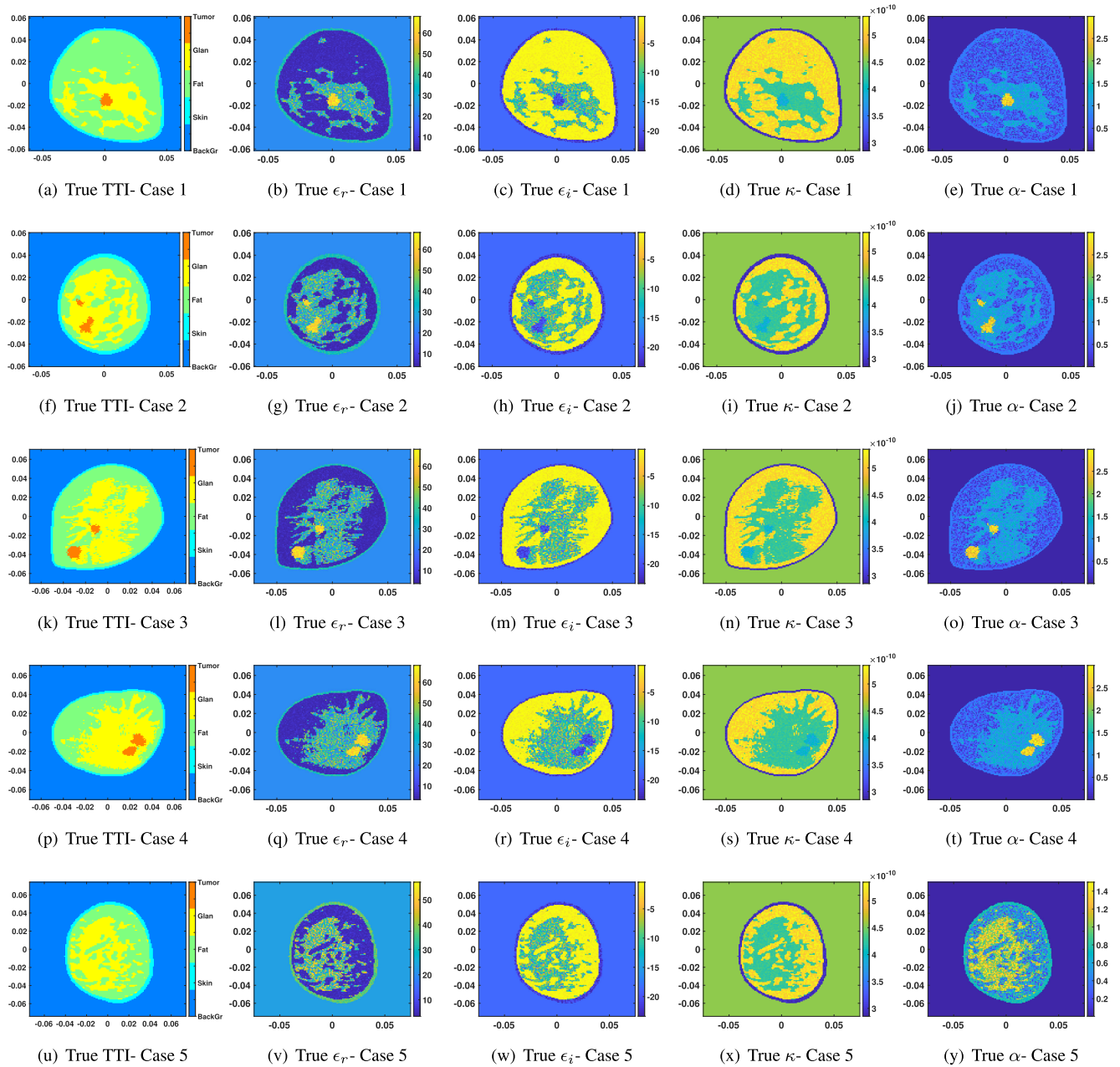
IEEE *Access*

FIGURE 2. Flowchart of a deep learning network for tissue-type classification and uncertainty quantification. The input is quantitative reconstructions of dielectric and/or ultrasonic properties and the output for testing the U-net are the tissue-type and uncertainty quantification images. The training mask for this phantom is also shown as the output of U-net for training. The training mask has five channels corresponding to the background, skin, fat, glandular and tumor masks. The number of channels are shown on top of each box.

recordings was modified for our application. The flow-chart of the particular U-net utilized is shown in Fig 2. As can be seen in this flowchart, the left (input) side of the U-net corresponds to repeated convolutional and downsampling layers. It should be noted that the number of feature channels is doubled at each downsampling step. The right (output) side of the U-net corresponds to the deconvolution and upsampling layers. The number of feature channels is reduced by half at each step of upsampling. For the final layer, a 1×1 convolution (with "softmax" activation) is used to map 32 feature channels to 5 channels corresponding to the number of chosen regions in each breast. As previously described, we have chosen five regions, namely the background plus four tissue-types: skin, fat, fibroglandular, and tumor.

Training of our deep learning networks was achieved using both MWT and/or UT images obtained from the previously described MRI-derived data-set. That is, the input to the CNN are the images of the quantitative reconstructions of the dielectric and/or ultrasonic properties obtained using GNI on the synthetic scattered-field data for each of the numerical breast phantoms. The U-net maps these input images to an output image which is then compared to the true tissue-type of the numerical breast phantom. The categorical cross-entropy error is used as the loss-function for training. Each of the background and four tissue-types predicted by the U-net are represented by a binary mask output by one of the five channels. For example in the tumor mask, the value of pixels

corresponding to tumor regions is set to be one (*i.e.,* the probability of being a tumor on that pixels is one) whereas the values of other pixels are set to be zero (*i.e.,* zero probability of being a tumor). Example input and output images for one of the phantoms are shown in Fig 2 (the output of training is denoted by the "training mask"). Each U-net is trained based on the input of dielectric properties, ultrasonic properties, as well as their combination.

After the U-net is trained, we tested it with several breast models that were not used for training. The output of the U-net when tested with a particular breast phantom has five channels (each a complete image) containing the probability that a pixel corresponds to the particular region associated with that channel. For example, the last channel shows the probability of a pixel in the image being a tumor. At each pixel the tissue-type (channel) with the highest probability is taken to be the predicted tissue-type in the TTI and this highest probability is also stored in a probability image. This probability image estimates the confidence we have in choosing a particular tissue-type for each pixel. The reconstruction of TTI and probability image for one of the breast phantoms based on the input of dielectric properties and/or the input of ultrasonic properties are shown in Fig 2. Note that each pixel of the input has a quantitative value for the particular property it represents. However, each pixel of the output corresponds to a particular tissue-type such as fat, glandular and tumor (a discrete quantitative value).

IEEE *Access*

P. Mojabi *et al.*: Tissue-Type Classification With Uncertainty Quantification of Microwave and Ultrasound Breast Imaging
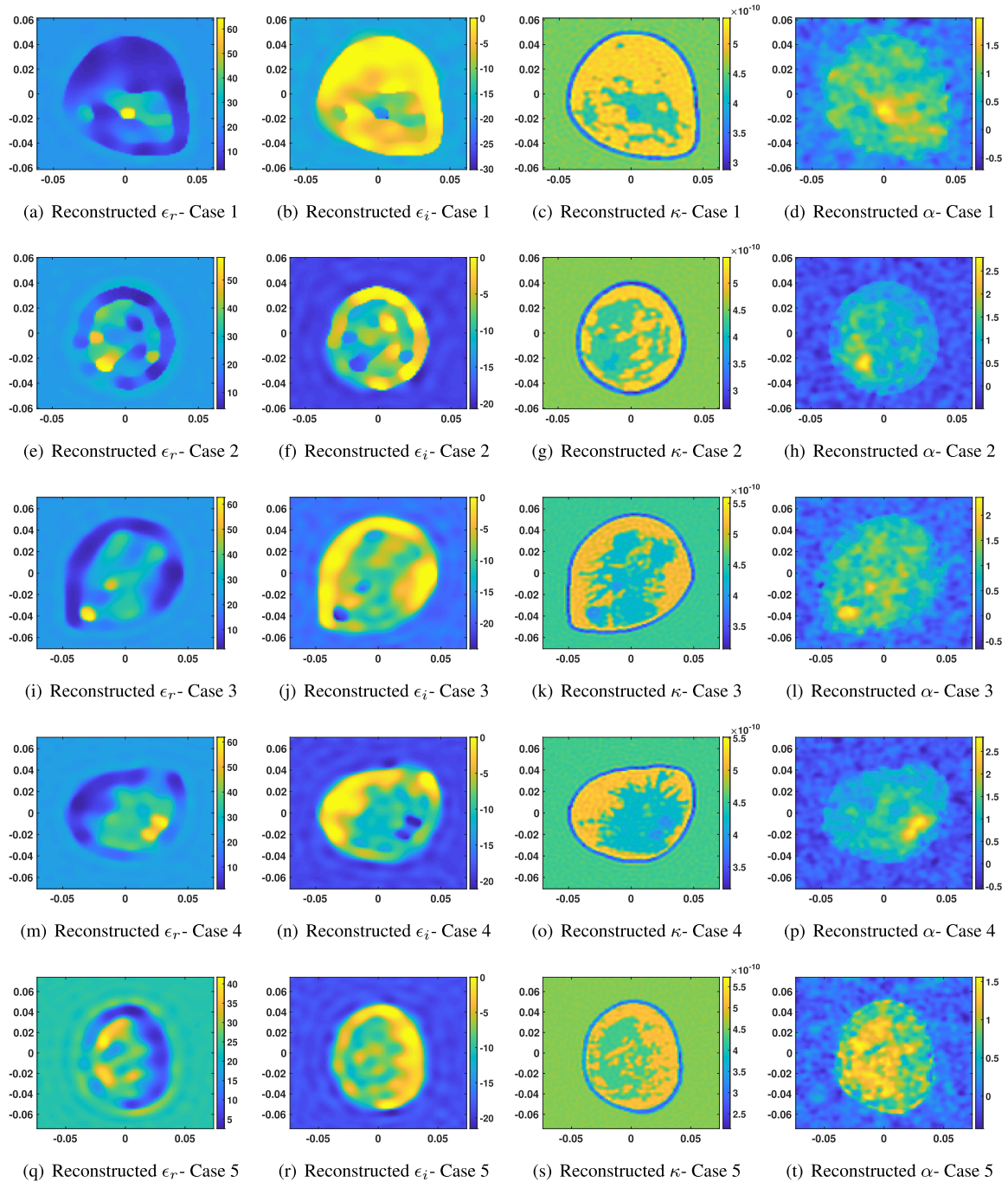
FIGURE 3. Five cases of MRI-based numerical breast phantoms. Each row consists of five figures for a given case: true TTI, true dielectric properties (real and imaginary parts), and true ultrasonic properties (compressibility and attenuation).

IV. RESULTS

Five of the different numerical MRI-based breast models used for testing, with particular tumor instances, are shown in different rows of Fig 3. The last row is a case with no tumor present and was used to test the robustness of the technique.

The true TTI and corresponding dielectric and ultrasonic properties for each case are shown in a particular column of Fig 3. The multiplicatively regularized GNI algorithm is used as a non-linear inversion algorithm for the reconstruction of dielectric and ultrasonic properties [20], [23].
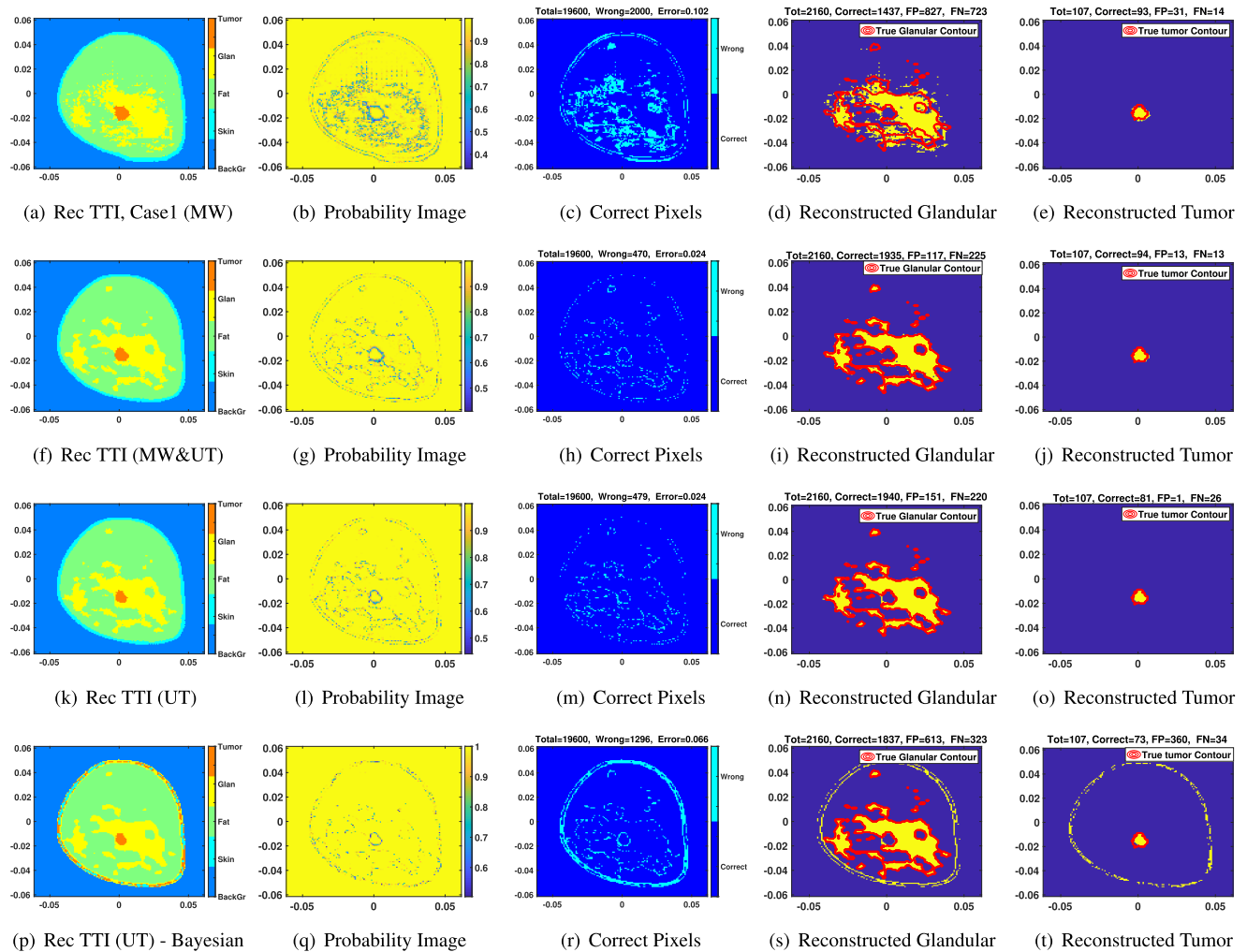
The quantitative reconstructions of the dielectric and ultrasonic properties for each of these breast phantom cases are shown in a particular row and column of Fig 4. To avoid inverse crime, the meshes used in the inversion algorithm (for both MWT and UT) are different from those used in the generation of the simulated data to be inverted. The reconstructed dielectric and ultrasonic properties are then interpolated to the meshes used for the generation of the simulated data (true profile). Furthermore, the scattered data for both UT and MWT are contaminated with five percent noise according to the formula presented in [43].

P. Mojabi *et al.*: Tissue-Type Classification With Uncertainty Quantification of Microwave and Ultrasound Breast Imaging

IEEE *Access*

FIGURE 4. Reconstruction of dielectric and ultrasonic properties of five breast cases. Each row consists of four reconstructed images. The first two images in each row correspond to the reconstruction of dielectric properties (real and imaginary parts of the relative complex permittivity) and the last two images in each row correspond to the reconstruction of ultrasonic properties (compressibility and attenuation).

In the following, the reconstruction of tissue type as well as uncertainty quantification (probability images) using the reconstruction of dielectric and/or ultrasonic properties are shown for the same five cases. The CNN U-net tissue-type reconstructions are also compared with the tissue-type reconstructions obtained using our previous Bayesian approach in Sections IV-A.3 and IV-B.3. The multi-variate normal probability density function is used in applying the Bayesian method [25]. The single frequency reconstruction of dielectric properties is tested in Section IV-E. It should be noted that the U-net is trained based on the images obtained from the simultaneous frequency inversion. The U-net which is trained with breast phantoms having tumors is also tested with a phantom that does not have any tumors in the Section IV-F.

IEEE *Access*

P. Mojabi *et al.*: Tissue-Type Classification With Uncertainty Quantification of Microwave and Ultrasound Breast Imaging

FIGURE 5. The reconstruction of TTI, probability image, correct pixels, glandular and tumor regions for the breast phantom-Case 1. The first row corresponds to the results based on dielectric properties. The second row corresponds to the results based on dielectric and ultrasonic properties. The third row corresponds to the results based on the ultrasonic properties. The last row corresponds to the results based on ultrasonic properties using Bayesian approach. (Note that the false positive and false negative are denoted by FP and FN.)

A. CASE 1

The true TTI for this case is shown in Fig 3a. The true dielectric properties and ultrasonic properties for this phantom are also shown in Figs 3 (b,c) and Figs 3 (d,e), respectively. The reconstruction of dielectric properties and ultrasonic properties for this case are shown in Figs 4 (a,b) and Figs 4 (c,d), respectively. As can be seen, the resolution of the reconstructed ultrasonic property images is higher than the reconstructed dielectric property images due to the smaller wavelength used for the ultrasound imaging. The reconstructions of the predicted TTI and the associated uncertainty quantification for this phantom under different scenarios are discussed below.
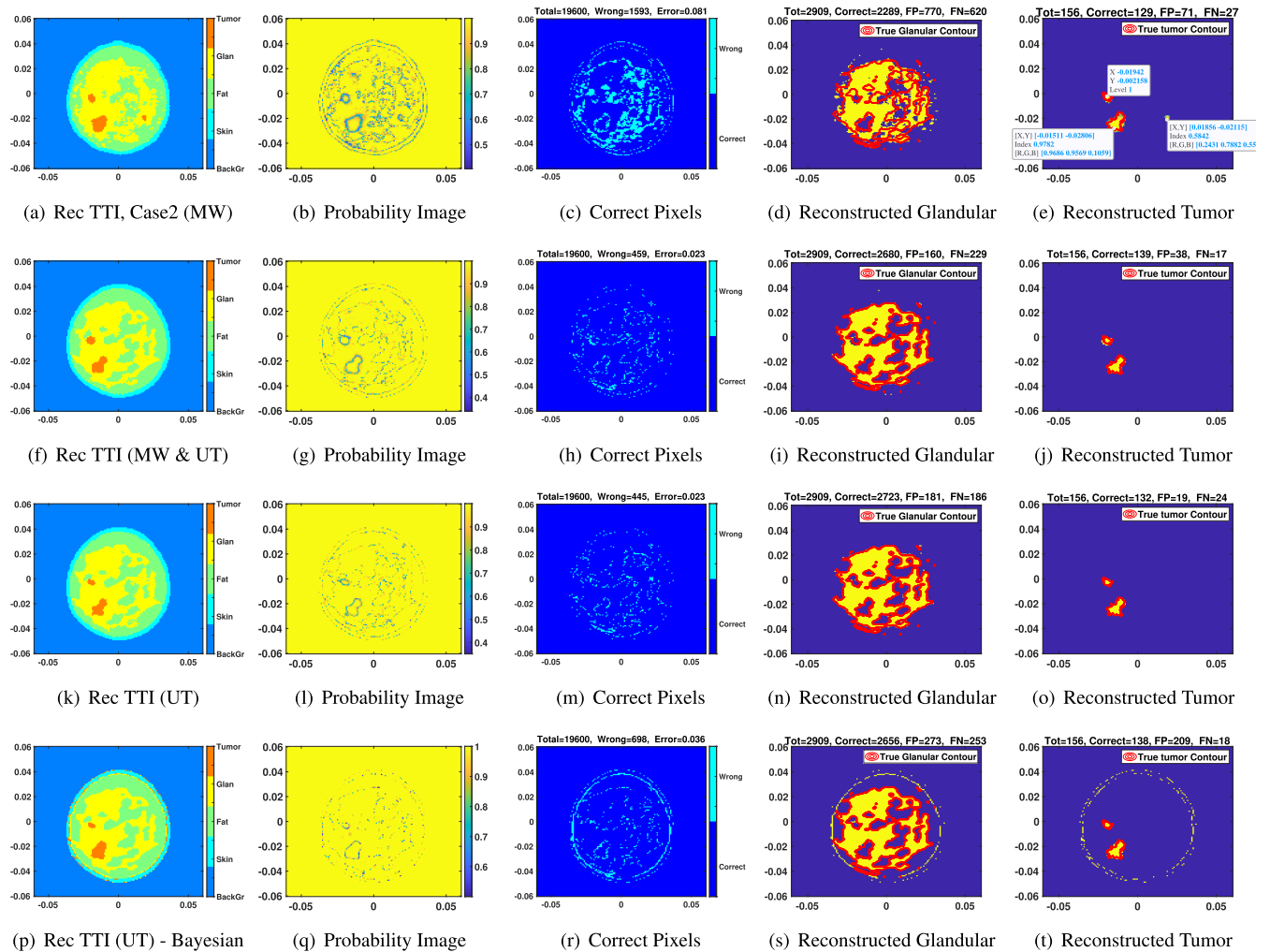
1) TWO DIELECTRIC PROPERTIES

The reconstruction of the TTI and uncertainty quantification based using only the two dielectric properties (*i.e.*, real and imaginary parts of complex permittivity) as input for the

U-net are shown in Figs 5 (a,b). The correct pixels as well as the reconstructed glandular and tumor regions are shown in Figs 5 (c,d,e).

2) TWO DIELECTRIC AND TWO ULTRASONIC PROPERTIES

The reconstruction of the TTI and uncertainty quantification based on using both the two dielectric (*i.e.*, complex permittivity) and the two ultrasonic properties (*i.e.*, compressibility and attenuation) as input for the U-net are shown in the Figs 5 (f,g). The correct pixels and the reconstructed glandular and tumor regions are shown in Figs 5 (h.i.j). As can be seen in the correct pixel images, the overall error is reduced from 0.102 to 0.024, when we use the U-net trained by both ultrasonic and dielectric properties instead of being only trained with microwave properties. One reason for this is that the wavelength used in the ultrasound imaging is much smaller than that of the microwave imaging. For example, the fine details of the glandular region is more clear in the

P. Mojabi *et al.*: Tissue-Type Classification With Uncertainty Quantification of Microwave and Ultrasound Breast Imaging

IEEE *Access*

FIGURE 6. The reconstruction of TTI, probability image, correct pixels, glandular and tumor regions for the breast phantom-Case 2. The first row corresponds to the results based on dielectric properties. The second row corresponds to the results based on dielectric and ultrasonic properties. The third row corresponds to the results based on the ultrasonic properties. The last row corresponds to the results based on ultrasonic properties using Bayesian approach.

reconstructed compressibility compared to the reconstructions of the complex permittivity shown in Fig 4. The false positive and false negative for both glandular region and tumor region are also decreased as shown in Figs 5 (d,e) and Figs 5 (i,j).

3) DEEP LEARNING VS BAYESIAN METHOD FOR TWO ULTRASONIC PROPERTY IMAGES
We now compare the deep learning U-net reconstructed TTI and uncertainty quantification with using the Bayesian method described in [25] when using two ultrasonic properties (*i.e.,* compressibility and attenuation). The results of tissue-type classification, uncertainty quantification, correct pixels, reconstructed glandular and tumor regions using U-net and the Bayesian method are shown in the third and fourth rows of Fig 5. As can be seen, the result of tissue-type classification obtained from the U-net is more accurate than the result obtained from Bayesian method. For the example shown, the overall error of classification using U-net and

Bayesian method are 0.024 and 0.066, respectively, as shown in Figs 5 (m,r). False positive and false negative for tumor and glandular regions using the Bayesian method are higher than the FP and FN using the trained U-net as shown in Figs 5 (s,t) and Figs 5 (n,o). In the Bayesian method, many skin pixels are wrongly predicted as a glandular or tumor.

B. CASE 2
The true TTI, true dielectric and true ultrasonic property images are shown in the second row of Fig 3. The reconstruction of dielectric properties and ultrasonic properties for this case are shown in the second row of Fig 4. The reconstructions of the predicted TTI and uncertainty quantification for this phantom under different scenarios are discussed below.

1) TWO DIELECTRIC PROPERTIES
The results of tissue-type classification and uncertainty quantification based on the input of two dielectric properties for the U-net are shown in Figs 6 (a,b). The correct pixels

IEEE Access

P. Mojabi *et al.*: Tissue-Type Classification With Uncertainty Quantification of Microwave and Ultrasound Breast Imaging
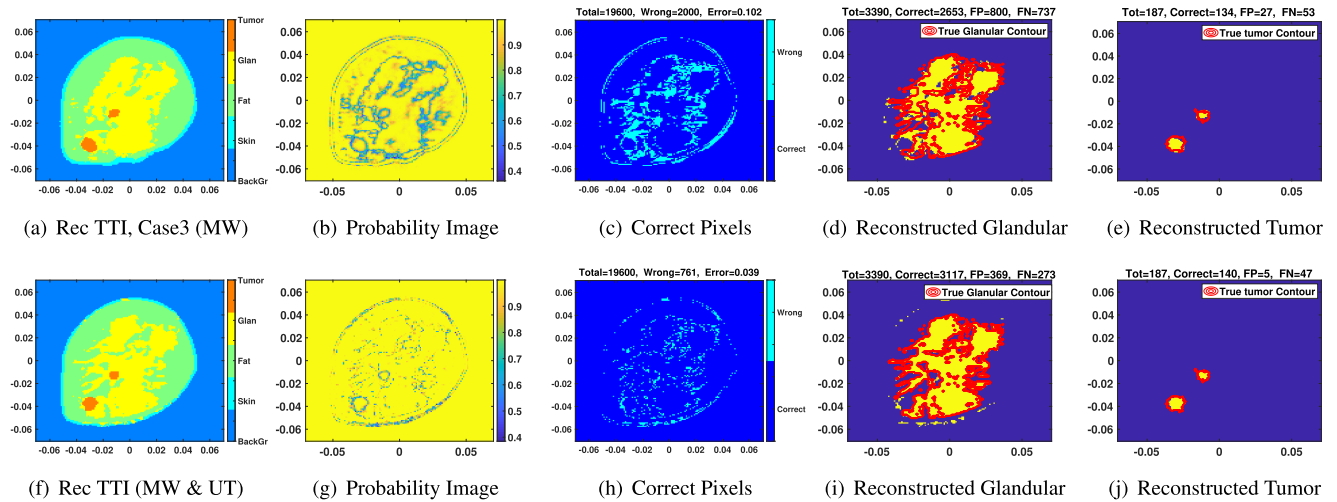
FIGURE 7. The reconstruction of TTI, probability image, correct pixels, glandular and tumor regions for the breast phantom–Case 3. The first row corresponds to the results based on dielectric properties. The second row corresponds to the results based on dielectric and ultrasonic properties.

and reconstructed glandular and tumor regions are shown in Figs 6 (c,d,e). Comparing the reconstruction of TTI in Fig 6 (a) with the true TTI in Fig 3 (f), it can be seen that one region on the right side of the reconstructed TTI is wrongly chosen as a tumor region. This is due to the fact that the quantitive reconstruction of complex permittivity for this region is close to the quantitative value corresponding to tumor tissue as shown in Figs 4 (e,f). However, the good point is that the probability of the pixels in that region is low as can be seen in the uncertainty quantification. For example, the probability of one of the pixels in this region wrongly chosen as a tumor is about 0.5842 and the probability of two pixels which are truly chosen as a tumor are high (1 and 0.9782) as shown in Fig 6e.

2) TWO DIELECTRIC AND TWO ULTRASONIC PROPERTIES
The results of tissue-type classification and uncertainty quantification based on using two dielectric and two ultrasonic properties as the input for the U-net are shown in Figs 6 (f,g). The correct pixels and reconstructed glandular and tumor regions are shown in Figs 6 (h,i,j). Comparing the result in this section with the result obtained based on using only dielectric properties, we can see that the region which is wrongly chosen as a tumor in the previous case is now correctly detected as a glandular region. Furthermore, the overall error in the tissue classification has decreased from 0.081 to 0.023 as shown in Figs 6 (c,h) and the false positive and false negative for glandular and tumor regions are also reduced as shown in Figs 6 (d,e) and Figs 6 (i,j).

3) DEEP LEARNING VS BAYESIAN METHOD FOR TWO ULTRASONIC PROPERTY IMAGES
The comparison between the reconstructions of the TTI as well as probability image using deep learning and Bayesian method are shown in the third and fourth rows of Fig 6, respectively. As can be seen, the reconstruction of TTI using the deep learning method is again more accurate than the

result obtained from the Bayesian method. For example, the overall error in the reconstruction of the TTI using deep learning and the Bayesian method are 0.023 and 0.036, respectively. The number of false positive and false negative pixels for the glandular region using deep learning method are 181 and 186 as shown in Fig 6 n. However, these numbers using Bayesian method are 273 and 253.

C. CASE 3
The true TTI, true dielectric and true ultrasonic properties for this case are shown in the third row of Fig 3. This model has two tumors with different sizes. Approximating the tumors with a circular shape, the radius of the smaller tumor is about 4 [mm] which corresponds to $0.42\lambda_{min}$ in UT and $0.13\lambda_{min}$ in MWT (λ_{min} is the minimum wavelength of the ultrasonic wave or microwaves in the background medium based on their respective frequencies of operation). The radius of the other tumor is about 6 [mm] corresponding to $0.64\lambda_{min}$ in UT and $0.19\lambda_{min}$ in MWT. The reconstruction of dielectric properties and ultrasonic properties are shown in the third row of Fig 4. The results of tissue-type classification and uncertainty quantification based on the input of two dielectric properties and four dielectric and ultrasonic properties are shown in the first and second rows of Fig 7. As can be seen, the two tumors are detected in both cases. The glandular region is better detected when both ultrasonic and dielectric properties are used as shown in Figs7 (d,i). For this example, the number of false positive and false negative pixels for the glandular region obtained from using only dielectric properties are 800 and 737. However, these numbers are reduced to 369 and 273 when both dielectric and ultrasonic properties are used as the input of U-net for tissue classification.

D. CASE 4
The true TTI, true dielectric and true ultrasonic properties are for this case are shown in the fourth row of Fig 3.
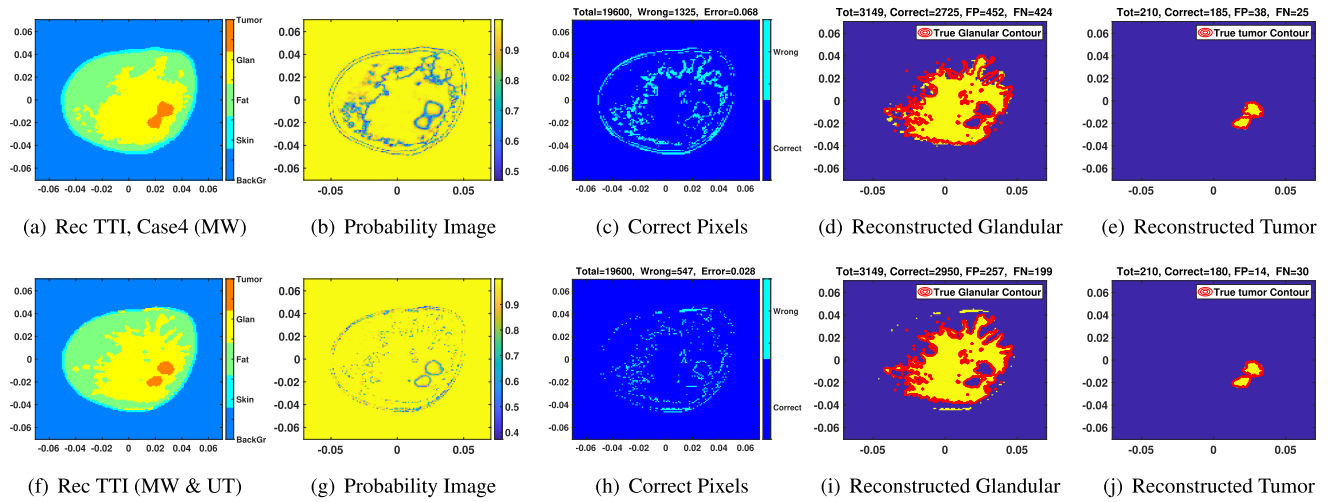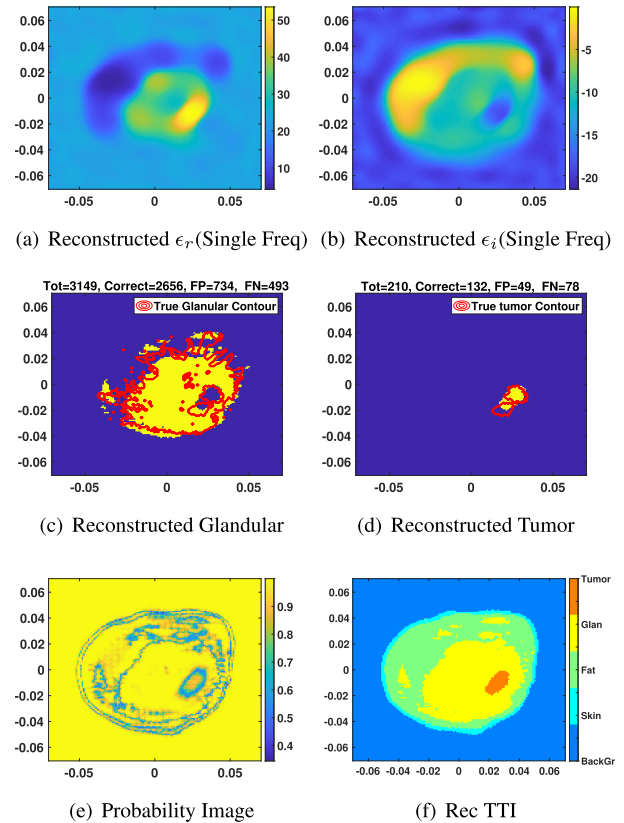
FIGURE 8. The reconstruction of TTI, probability image, correct pixels, glandular and tumor regions for the breast phantom-Case 4. The first row corresponds to the results based on dielectric properties. The second row corresponds to the results based on dielectric and ultrasonic properties.

The reconstruction of dielectric properties and ultrasonic properties are shown in the fourth row of Fig 4. The results of tissue type classification and uncertainty quantification based on the input of two dielectric properties and four dielectric and ultrasonic properties are shown in the first and second rows of Fig 8.
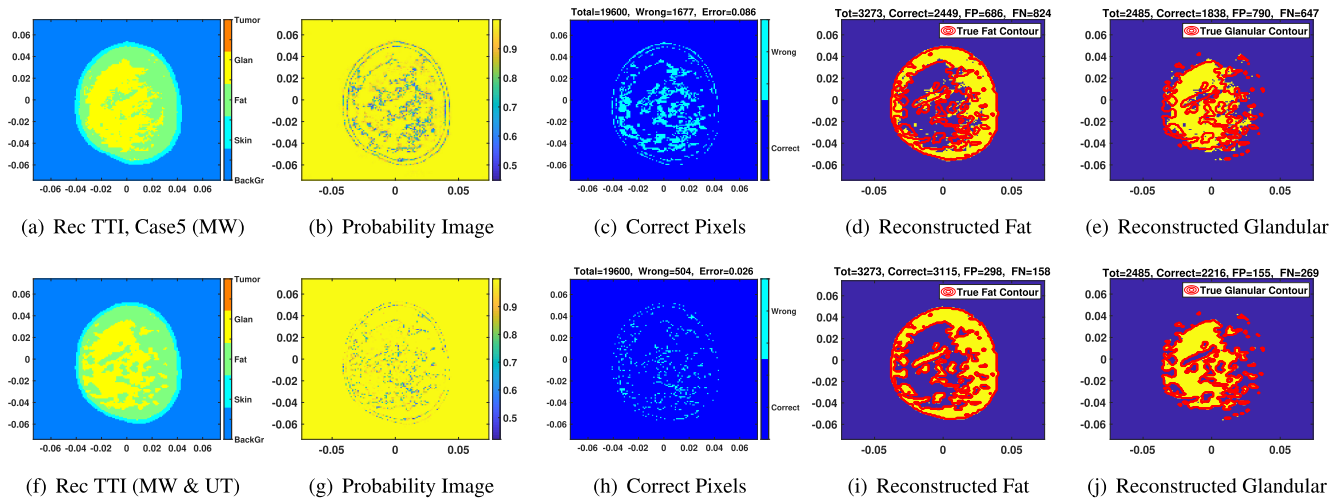
E. CASE 4 - MW SINGLE FREQUENCY INVERSION

The true TTI, and true dielectric properties for this phantom are shown in the fourth row of Figs 3. As was explained in Section II-B, three frequencies are simultaneously utilized to create the dielectric properties of the breast phantoms. The reason for using simultaneous frequency inversion is to increase the amount of data leading to a more accurate reconstruction of the dielectric properties. The training microwave images for the U-net are also based on the reconstruction of dielectric properties obtained from the simultaneous frequency inversion.

In this section, we test the trained U-net based on the input of dielectric properties obtained from the single frequency inversion. The results of the reconstruction of dielectric properties for this phantom based on the single frequency (1 GHz) inversion are shown in the first row of Fig 9. The reconstruction of the TTI, probability image, glandular and tumor regions are shown in the second and third rows of Fig 9. As can be seen in Fig 9 f, the TTI is properly reconstructed, although the trained U-net for dielectric properties is based on the simultaneous frequency inversion (using three frequencies). It should be noted that the reconstruction of the dielectric properties using simultaneous frequency inversion shown in Figs 4 (m,n) is more accurate than the reconstruction based on the single frequency inversion shown in the first row of Fig 9. For example, the two tumors are more distinguishable using the simultaneous frequency inversion as compared to the single frequency inversion. Thus, the reconstruction of the TTI is also more accurate using the input of dielectric

FIGURE 9. Reconstruction of TTI based on dielectric properties obtained from single frequency inversion. The first row is the reconstructed real and imaginary parts of complex permittivity using single frequency inversion. The second row shows the reconstruction of glandular and tumor regions. The last row corresponds to the reconstruction of TTI and probability image.

properties obtained from simultaneous frequency inversion. For example, the number of correct, false positive and false negative pixels for the tumor region obtained from single

IEEE *Access*

P. Mojabi *et al.*: Tissue-Type Classification With Uncertainty Quantification of Microwave and Ultrasound Breast Imaging

FIGURE 10. The reconstruction of TTI, probability image, correct pixels, fat and glandular regions for the breast phantom-Case 5. This phantom does not have any tumor. The first row corresponds to the results based on dielectric properties. The second row corresponds to the results based on dielectric and ultrasonic properties.

frequency are 132, 49 and 78 respectively. These numbers for the tissue-type reconstruction based on the input of dielectric properties obtained from simultaneous frequency inversion are 185, 38 and 25.

F. CASE 5 (PHANTOM WITH NO TUMOR)

All the phantoms used for the training of the various U-nets have different numbers of tumors ranging from 1 to 3 with different sizes and different locations within the breast. In this example, we want to test the trained network for a case that does not have any tumor. The true TTI, true dielectric and true ultrasonic properties of this phantom are shown in the last row of Fig 3. As can be seen in the true TTI of this phantom, it does not have any tumor region but we still keep the tumor in the colorbar of this image. The reconstruction of dielectric properties and ultrasonic properties for this case are shown in the last row of Fig 4. The results of the reconstruction of the TTI, uncertainty quantification, correct pixels, fat and glandular regions based on the input of two dielectric properties and four dielectric and ultrasonic properties are shown in the first and second rows of Fig 10. As can be seen in the reconstructed TTI in Figs 10 (a,f), although the trained U-net has never seen breast phantoms having no tumors, there is no region detected as a tumor in the reconstruction of the TTI.

V. CONCLUSION

We have proposed a framework for tissue classification and uncertainty quantification for a breast imaging application based on a deep learning approach. The deep learning network is trained based on the input of quantitative images of dielectric and ultrasonic properties of the OI and maps this input to a predicted tissue-type image. To train and test the U-net, eight models of numerical MRI-based breast phantoms are utilized for both MWT and UT. For each model, we create fifty different phantoms with different numbers, sizes and

positions of tumor in the breast phantom. The Gauss-Newton inversion is used as a full-wave reconstruction algorithm for the reconstruction of ultrasonic and dielectric properties of the object of interest. The results of tissue-type imaging and the associated uncertainty quantification using the input of dielectric properties, ultrasonic properties and their combination are shown using different types of numerical breast phantoms. It is shown that this deep learning technique can provide promising results of TTI and uncertainty quantification. This deep learning technique is also compared with a previously studied Bayesian method and it shows a significant enhancement in the reconstruction of the TTI. The robustness of this technique is also checked with a breast phantom with no tumor regions and the reconstruction obtained from single frequency inversion.

VI. ACKNOWLEDGMENT

REFERENCES

[1] P. Mojabi and J. LoVetri, "Experimental evaluation of composite tissue-type ultrasound and microwave imaging," *IEEE J. Multiscale Multiphys. Comput. Techn.*, vol. 4, pp. 119–132, 2019.

[2] C. Li, N. Duric, P. Littrup, and L. Huang, "*In vivo* breast sound-speed imaging with ultrasound tomography," *Ultrasound Med. Biol.*, vol. 35, no. 10, pp. 1615–1628, Oct. 2009.

[3] E. C. Fear, S. C. Hagness, P. M. Meaney, M. Okoniewski, and M. A. Stuchly, "Enhancing breast tumor detection with near-field imaging," *IEEE Microw. Mag.*, vol. 3, no. 1, pp. 48–56, Mar. 2002.

[4] N. Abdollahi, D. Kurrant, P. Mojabi, M. Omer, E. Fear, and J. LoVetri, "Incorporation of ultrasonic prior information for improving quantitative microwave imaging of breast," *IEEE J. Multiscale Multiphys. Comput. Techn.*, vol. 4, pp. 98–110, 2019.

[5] P. Mojabi and J. LoVetri, "Evaluation of balanced ultrasound breast imaging under three density profile assumptions," *IEEE Trans. Comput. Imag.*, vol. 3, no. 4, pp. 864–875, Dec. 2017.

P. Mojabi *et al.*: Tissue-Type Classification With Uncertainty Quantification of Microwave and Ultrasound Breast Imaging

IEEE *Access*

[6] M. Omer, P. Mojabi, D. Kurrant, J. LoVetri, and E. Fear, "Proof-of-concept of the incorporation of ultrasound-derived structural information into microwave radar imaging," *IEEE J. Multiscale Multiphys. Comput. Techn.*, vol. 3, pp. 129–139, 2018.

[7] N. Bayat and P. Mojabi, "Incorporating spatial priors in microwave imaging via multiplicative regularization," *IEEE Trans. Antennas Propag.*, vol. 68, no. 2, pp. 1107–1118, Feb. 2020.

[8] N. Duric, P. Littrup, L. Poulo, A. Babkin, R. Pevzner, E. Holsapple, O. Rama, and C. Glide, "Detection of breast cancer with ultrasound tomography: First results with the computed ultrasound risk evaluation (CURE) prototype," *Med. Phys.*, vol. 34, no. 2, pp. 773–785, Jan. 2007.

[9] X. Song, M. Li, F. Yang, S. Xu, and A. Abubakar, "Feasibility study of acoustic imaging for human thorax using an acoustic contrast source inversion algorithm," *J. Acoust. Soc. Amer.*, vol. 144, no. 5, pp. 2782–2792, Nov. 2018, doi: 10.1121/1.5078590.

[10] Z. Q. Zhang and Q. H. Liu, "Three-dimensional nonlinear image reconstruction for microwave biomedical imaging," *IEEE Trans. Biomed. Eng.*, vol. 51, no. 3, pp. 544–548, Mar. 2004.

[11] N. K. Nikolova, *Introduction to Microwave Imaging* (EuMA High Frequency Technologies Series). Cambridge, U.K.: Cambridge Univ. Press, 2017.

[12] P. M. Meaney, M. W. Fanning, D. Li, S. P. Poplack and K. D. Paulsen, "A clinical prototype for active microwave imaging of the breast," *IEEE Trans. Microw. Theory Techn.*, vol. 48, no. 11, pp. 1841–1853, Nov. 2000, doi: 10.1109/22.883861.

[13] L. M. Neira, B. D. Van Veen, and S. C. Hagness, "High-resolution microwave breast imaging using a 3-D inverse scattering algorithm with a variable-strength spatial prior constraint," *IEEE Trans. Antennas Propag.*, vol. 65, no. 11, pp. 6002–6014, Nov. 2017.

[14] M. Pastorino, *Microwave Imaging* (Wiley Series in Microwave and Optical Engineering). Hoboken, NJ, USA: Wiley, 2010.

[15] J. Mamou and M. L. Oelze, *Quantitative Ultrasound in Soft Tissues*. New York, NY, USA: Springer, 2013.

[16] R. Lavarello and M. Oelze, "A study on the reconstruction of moderate contrast targets using the distorted born iterative method," *IEEE Trans. Ultrason., Ferroelectr., Freq. Control*, vol. 55, no. 1, pp. 112–124, Jan. 2008.

[17] K. Wang, T. Matthews, F. Anis, C. Li, N. Duric, and M. Anastasio, "Waveform inversion with source encoding for breast sound speed reconstruction in ultrasound computed tomography," *IEEE Trans. Ultrason., Ferroelectr., Freq. Control*, vol. 62, no. 3, pp. 475–493, Mar. 2015.

[18] T. Sleasman, M. Boyarsky, M. F. Imani, T. Fromenteze, J. N. Gollub, and D. R. Smith, "Single-frequency microwave imaging with dynamic metasurface apertures," *J. Opt. Soc. Amer. B, Opt. Phys.*, vol. 34, no. 8, pp. 1713–1726, Aug. 2017.

[19] M. Haynes and M. Moghaddam, "Large-domain, low-contrast acoustic inverse scattering for ultrasound breast imaging," *IEEE Trans. Biomed. Eng.*, vol. 57, no. 11, pp. 2712–2722, Nov. 2010.

[20] M. Ostadrahimi, P. Mojabi, A. Zakaria, J. LoVetri, and L. Shafai, "Enhancement of Gauss-Newton inversion method for biological tissue imaging," *IEEE Trans. Microw. Theory Techn.*, vol. 61, no. 9, pp. 3424–3434, Sep. 2013.

[21] P. Mojabi and J. LoVetri, "Ultrasound tomography for simultaneous reconstruction of acoustic density, attenuation, and compressibility profiles," *J. Acoust. Soc. Amer.*, vol. 137, no. 4, pp. 1813–1825, Apr. 2015.

[22] N. Ozmen, R. Dapp, M. Zapf, H. Gemmeke, N. V. Ruiter, and K. W. A. van Dongen, "Comparing different ultrasound imaging methods for breast cancer detection," *IEEE Trans. Ultrason., Ferroelectr., Freq. Control*, vol. 62, no. 4, pp. 637–646, Apr. 2015.

[23] P. Mojabi and J. LoVetri, "Microwave biomedical imaging using the multiplicative regularized Gauss–Newton inversion," *IEEE Antennas Wireless Propag. Lett.*, vol. 8, pp. 645–648, 2009.

[24] A. J. Hesford and W. C. Chew, "Fast inverse scattering solutions using the distorted born iterative method and the multilevel fast multipole algorithm," *J. Acoust. Soc. Amer.*, vol. 128, no. 2, pp. 679–690, Aug. 2010.

[25] P. Mojabi and J. LoVetri, "Composite tissue-type and probability image for ultrasound and microwave tomography," *IEEE J. Multiscale Multiphys. Comput. Techn.*, vol. 1, pp. 26–35, 2016.

[26] O. Ronneberger, P. Fischer, and T. Brox, "U-Net: Convolutional networks for biomedical image segmentation," in *Medical Image Computing and Computer-Assisted Intervention*, N. Navab, J. Hornegger, W. M. Wells, and A. F. Frangi, Eds. Cham, Switzerland: Springer, 2015, pp. 234–241.

[27] V. Khoshdel, A. Ashraf, and J. LoVetri, "Enhancement of multimodal microwave-ultrasound breast imaging using a deep-learning technique," *Sensors*, vol. 19, no. 18, p. 4050, Sep. 2019.

[28] G. Chen, P. Shah, J. Stang, and M. Moghaddam, "Learning-assisted multimodality dielectric imaging," *IEEE Trans. Antennas Propag.*, vol. 68, no. 3, pp. 2356–2369, Mar. 2020.

[29] Z. Wei and X. Chen, "Deep-learning schemes for full-wave nonlinear inverse scattering problems," *IEEE Trans. Geosci. Remote Sens.*, vol. 57, no. 4, pp. 1849–1860, Apr. 2019.

[30] M. T. McCann, K. H. Jin, and M. Unser, "Convolutional neural networks for inverse problems in imaging: A review," *IEEE Signal Process. Mag.*, vol. 34, no. 6, pp. 85–95, Nov. 2017.

[31] I. T. Rekanos, "Neural-network-based inverse-scattering technique for online microwave medical imaging," *IEEE Trans. Magn.*, vol. 38, no. 2, pp. 1061–1064, Mar. 2002.

[32] V. Khoshdel, M. Asefi, A. Ashraf, and J. LoVetri, "Full 3D microwave breast imaging using a deep-learning technique," *J. Imag.*, vol. 6, no. 8, p. 80, Aug. 2020.

[33] G. Wang, W. Li, M. A. Zuluaga, R. Pratt, P. A. Patel, M. Aertsen, T. Doel, A. L. David, J. Deprest, S. Ourselin, and T. Vercauteren, "Interactive medical image segmentation using deep learning with image-specific fine tuning," *IEEE Trans. Med. Imag.*, vol. 37, no. 7, pp. 1562–1573, Jul. 2018.

[34] Y. Xie, Y. Xia, J. Zhang, Y. Song, D. Feng, M. Fulham, and W. Cai, "Knowledge-based collaborative deep learning for benign-malignant lung nodule classification on chest CT," *IEEE Trans. Med. Imag.*, vol. 38, no. 4, pp. 991–1004, Apr. 2019.

[35] L. Li, L. G. Wang, F. L. Teixeira, C. Liu, A. Nehorai, and T. J. Cui, "DeepNIS: Deep neural network for nonlinear electromagnetic inverse scattering," *IEEE Trans. Antennas Propag.*, vol. 67, no. 3, pp. 1819–1825, Mar. 2019.

[36] Y. A. Rahama, O. Al Aryani, U. A. Din, M. A. Awar, A. Zakaria, and N. Qaddoumi, "Novel microwave tomography system using a phased-array antenna," *IEEE Trans. Microw. Theory Techn.*, vol. 66, no. 11, pp. 5119–5128, Nov. 2018.

[37] S. P. Rana, M. Dey, G. Tiberi, L. Sani, A. Vispa, G. Raspa, M. Duranti, M. Ghavami, and S. Dudley, "Machine learning approaches for automated lesion detection in microwave breast imaging clinical data," *Sci. Rep.*, vol. 9, no. 1, pp. 1–12, Dec. 2019.

[38] A. Krizhevsky, I. Sutskever, and G. E. Hinton, "ImageNet classification with deep convolutional neural networks," in *Advances in Neural Information Processing Systems*, F. Pereira, C. J. C. Burges, L. Bottou, and K. Q. Weinberger, Eds. Red Hook, NY, USA: Curran Associates, 2012, pp. 1097–1105.

[39] K. Simonyan and A. Zisserman, "Very deep convolutional networks for large-scale image recognition," 2014, *arXiv:1409.1556*. [Online]. Available: http://arxiv.org/abs/1409.1556

[40] M. Omer and E. Fear, "Anthropomorphic breast model repository for research and development of microwave breast imaging technologies," *Sci. Data*, vol. 5, no. 1, Dec. 2018, Art. no. 180257.

[41] D. Kurrant, A. Baran, J. LoVetri, and E. Fear, "Integrating prior information into microwave tomography part 1: Impact of detail on image quality," *Med. Phys.*, vol. 44, no. 12, pp. 6461–6481, Dec. 2017. [Online]. Available: https://aapm.onlinelibrary.wiley.com/doi/abs/10.1002/mp.12585

[42] A. Abubakar, P. M. van den Berg, and J. J. Mallorqui, "Imaging of biomedical data using a multiplicative regularized contrast source inversion method," *IEEE Trans. Microw. Theory Techn.*, vol. 50, no. 7, pp. 1761–1771, Jul. 2002.

[43] A. Abubakar, P. M. van den Berg, and S. Y. Semenov, "A robust iterative method for born inversion," *IEEE Trans. Geosci. Remote Sens.*, vol. 42, no. 2, pp. 342–354, Feb. 2004.

[44] T. Rubaek, P. M. Meaney, P. Meincke, and K. D. Paulsen, "Nonlinear microwave imaging for breast-cancer screening using Gauss–Newton's method and the CGLS inversion algorithm," *IEEE Trans. Antennas Propag.*, vol. 55, no. 8, pp. 2320–2331, Aug. 2007.

IEEE *Access*

P. Mojabi *et al.*: Tissue-Type Classification With Uncertainty Quantification of Microwave and Ultrasound Breast Imaging

PEDRAM MOJABI received the M.Sc. and Ph.D. degrees in electrical engineering from the University of Manitoba, Winnipeg, MB, Canada, in 2014 and 2019, respectively. He is a Postdoctoral Fellow with the Department of Electrical and Computer Engineering, University of Manitoba. His current research interests are computational electromagnetics, computational ultrasonics, ultrasound tomography, microwave tomography, and multiphysics imaging. He is currently an Engineer in Training (EIT) at the Engineers Geoscientists Manitoba. From 2012 to 2014, he has served as the Vice-Chair of the IEEE Winnipeg Waves Chapter. In addition, he served as the Vice-President of the Electrical and Computer Engineering Graduate Student Association (ECE-GSA) at the University of Manitoba, from 2017 to 2019.

VAHAB KHOSHDEL (Student Member, IEEE) was born in Iran, in February 1989. He received the M.Sc. degree in mechatronic engineering from the Shahrood University of Technology, Iran, in 2013. He is currently pursuing the Ph.D. degree with the University of Manitoba, Canada. As a Research Assistant with the Electromagnetic Imaging Laboratory, he is exploring using deep learning techniques for microwave imaging. His main areas of research interest are deep learning, machine learning, medical imaging, robotics, and control systems.

JOE LOVETRI (Senior Member, IEEE) received the Ph.D. degree in electrical engineering from the University of Ottawa, in 1991. From 1984 to 1986, he was an EMI/EMC Engineer with the Sperry Defense Division, Winnipeg. From 1986 to 1988, he was a TEMPEST Engineer with the Communications Security Establishment, Ottawa. From 1988 to 1991, he was a Research Officer with the Institute for Information Technology, National Research Council of Canada. His academic career began in 1991, when he joined the Department of Electrical and Computer Engineering, The University of Western Ontario, where he remained until 1999. From 1997 to 1998, he spent a sabbatical year at the TNO Physics and Electronics Laboratory, The Netherlands, doing research in time-domain computational methods and ground-penetrating RADAR. In 1999, he joined the University of Manitoba, where he is currently a Professor and the Head of the Department of Electrical and Computer Engineering. From 2004 to 2009, he was the Associate Dean of the Research and Graduate Programs with the Faculty of Engineering. His current research interests include computational electromagnetics, inverse problems, microwave and ultrasound imaging, and biomedical imaging. In 1993, he was a recipient of the URSI Young Scientist Award, the 2000 IEEE EMC Best Symposium Paper Award, the University of Manitoba Rh Award for Outstanding Contributions to Scholarship and Research in the applied sciences in 2002, and the 2007 ACES Outstanding Paper Award. From 2005 to 2009, he was the National Representative for Commission E on the Canadian National Committee of URSI. He has been the Chapter Chair of the IEEE EMC Ottawa Chapter and the Winnipeg Waves Chapter (AP/MTT). He has been a registered Professional Engineer since 1994.

• • •